

# Journal Pre-proof

Hollow ni-p amorphous alloy nanospheres: An efficient catalyst for sugars hydrogenation to polyols

Yong Yang, Huajun Gu, Qingxiao Zhang, Fang Zhang, Hui Li



PII: S0920-5861(20)30225-X  
DOI: <https://doi.org/10.1016/j.cattod.2020.04.031>  
Reference: CATTOD 12810  
To appear in: *Catalysis Today*  
Received Date: 10 January 2020  
Revised Date: 19 March 2020  
Accepted Date: 8 April 2020

Please cite this article as: { doi: <https://doi.org/>

This is a PDF file of an article that has undergone enhancements after acceptance, such as the addition of a cover page and metadata, and formatting for readability, but it is not yet the definitive version of record. This version will undergo additional copyediting, typesetting and review before it is published in its final form, but we are providing this version to give early visibility of the article. Please note that, during the production process, errors may be discovered which could affect the content, and all legal disclaimers that apply to the journal pertain.

© 2020 Published by Elsevier.

# Hollow Ni-P amorphous alloy nanospheres: an efficient catalyst for sugars hydrogenation to polyols

Yong Yang<sup>1</sup>, Huajun Gu<sup>1</sup>, Qingxiao Zhang, Fang Zhang\*, Hui Li\*

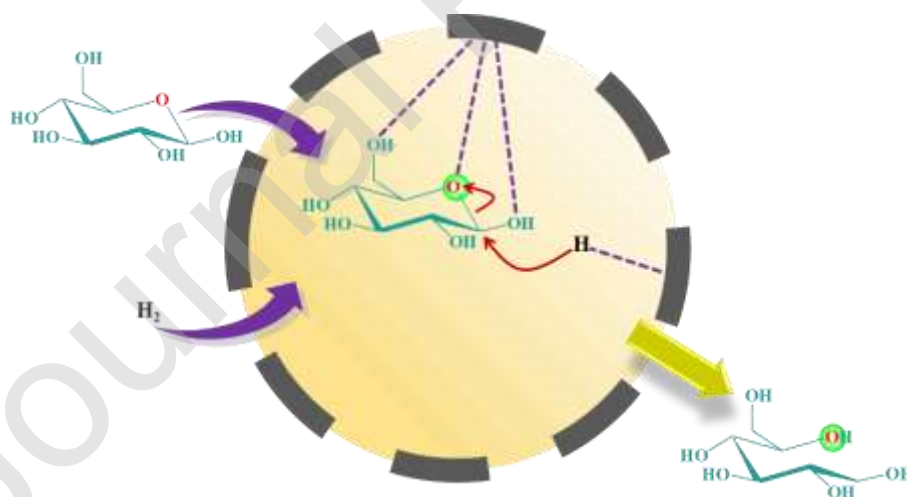
*Education Ministry Key Lab of Resource Chemistry and Shanghai Key Laboratory of Rare Earth Functional Materials, Shanghai Normal University, Shanghai 200234, PR China*

\* Corresponding author. Tel: +86 21 64323578; Fax: +86 21 64322272.

*E-mail address:* [lihui@shnu.edu.cn](mailto:lihui@shnu.edu.cn) (H. Li) [zhangfang@shnu.edu.cn](mailto:zhangfang@shnu.edu.cn) (F. Zhang)

<sup>1</sup> These authors contributed equally to this work.

## Graphical abstract



## Highlights

- ► Hollow Ni–P amorphous alloy nanospheres were prepared by electroless plating method.
- ► Such hollow catalyst showed a good potential in hydrogenation of sugars to polyols.
- ► Such hollow catalyst has the advantages of easy handling and accessibility.
- ► Such hollow catalyst provides more active sites for catalytic reaction.
- ► Such hollow catalyst possesses more electron-enriched inner surface.

### Abstract

In this paper, hollow Ni–P nanospheres (NSs) are prepared through Ni electroless plating on the Au-activated silica NSs externally covered by aminopropyl moieties, followed by removing the silica template with sodium hydroxide. With various characterizations, the resulting hollow Ni–P NSs are identified to be amorphous alloy. During liquid-phase hydrogenation of sugars to sugar alcohols, the hollow Ni–P amorphous alloy NSs delivered much superior catalytic performances to the commercial Raney Ni catalyst, showing a good potential in practical applications. Of particular interest is the unique

hollow chamber structure of the hollow Ni–P amorphous alloy NSs, which allows for improving catalytic activity and durability relative to those associated with the dense Ni–P amorphous alloy NSs. This work demonstrated that such hollow Ni materials with nanoporous chamber structure displayed advantages such as easy experimental handling and high accessibility for the reactants in liquid-phase reaction, more Ni active sites, as well as the existence of more electron-enriched inner surface, which is essential to provide highly efficient catalysts for some reactions.

**Keywords:** Ni–P amorphous alloy catalyst; Hollow nanospheres; Biomass transformation; Sugar hydrogenation; Polyols

## 1. Introduction

The production of fuels, chemicals and materials from renewable and abundant biomass resources has drawn immense attention in recent years as it possesses the possibility of using carbon neutral technologies to tackle global energy and environmental problems [1-5]. In viewpoint of atom economy, biomass materials are more desirable to be converted into oxygen-containing chemicals rather than hydrocarbon fuels due to their relatively high oxygen content [6]. In this respect, polyols derived from biomass resources are versatile molecules those have found a wide variety of applications [7]. In fact,

sugars can be facilely obtained from biomass resources, primarily starch [8-10] and even cellulose [11,12], through enzymatic hydrolysis bioprocesses. Therefore, the catalytic hydrogenation of naturally occurring sugars is an environmentally-friendly route to the production of the corresponding polyols. Among polyols from biomass, sorbitol, a hexitol, one of the top 12 biobased building blocks listed by the U.S. Department of Energy [13], is a valuable platform chemical that can be facilely transformed by straightforward methods into fuels or chemicals [1,14]. Nowadays, almost all existing sorbitol production processes are usually based on the hydrogenation of glucose catalyzed by metallic catalysts (Scheme 1) [15-23]. Currently, Raney Ni is mainly adopted in this industrial process [24]. However, the process is usually ineffective and may give rise to problems of environmental pollution resulting from the alkali leaching of Ni–Al alloy. In addition, the leaching of nickel during hydrogenation and the low activity make this catalyst less profitable, because a refilling of the catalyst and a purification of product to remove residual Ni are necessary, which eventually render this process economically less attractive [25]. Amorphous alloys, a kind of non-equilibrium metastable materials in thermodynamics with long-range disordered but short-range ordered structure, have attracted growing attention from both academia and industry because of their superior catalytic properties in comparison with the crystalline counterparts [26-28]. In general, M–B and M–P amorphous alloys are the most thoroughly studied [27]. Compared with M–B, M–P amorphous alloys

displayed much higher hydrogenation activity, including sugar hydrogenation to sugar alcohol [29,30], due to more highly unsaturated metal active sites promoted by alloying with P [27]. Although Ni–P amorphous alloy has proved to be a potential alternative to Raney Ni in liquid-phase glucose hydrogenation to sorbitol [31], there is still space to enhance the reactivity through controlling over its morphology, which will result in enhanced intrinsic activity, increased surface-active area, and an improved adsorption model of substances on the surface of catalysts [28].

In recent years, hollow structures have captured extensive attention owing to their potential applications in adsorption, microelectronics, photonics, as well as catalysis [32]. In the domain of catalysis, hollow metallic nanospheres (NSs) with permeable shell represent a new class of efficient catalysts because they offer some advantages over their dense counterparts in terms of increased surface area, low density, easy recovery, self-supporting capacity, cost reduction, and surface permeability [33-35]. Presently, a series of hollow amorphous alloy NSs have been fabricated based on soft-templating approach, in which the “soft” templates (*e.g.*, composite vesicle) are coated with metals by an interfacial reduction reaction [36-38]. However, this method is synthetically challenging, because the vigorous and exothermic reduction of metal precursors usually damages the architectures of the formed surfactant-directed assembly. Strategies based on the mechanisms of galvanic replacement have also been developed to fabricate hollow metal structures [39], which are more

facile and cost-effective since the templates could act as a reducing agents to produce metal shells and no additional steps are needed to remove the templates. Nevertheless, the synthesis of hollow metal NSs is limited mainly to noble metals or precious metal-containing alloys [40] by this synthesis strategy and thus their practical applications are limited due to the high cost. Adopting polystyrene beads as hard template to produce hollow Ni–B amorphous alloy was first introduced by Qiao's group, which displays advantages in its specific topological stability, veracity, predictability and controllability [41]. For achieving hollow metal structures, however, multistep surface activation are often necessary due to the weak affinity of the hydrophobic polymer host to nickel cations, complicating the preparation process. Because of surface hydrophilicity, silica NSs can act as promising hosts for depositing Ni–P amorphous alloy. Herein, we designed a novel approach to synthesizing hollow Ni–P amorphous alloy NSs by a combination of silica NSs templating and electroless plating (Scheme 2). Silica NSs externally covered by aminopropyl moieties were first fabricated by co-condensation method. The amine-functionalized host materials were activated with Au and then coated with Ni–P amorphous alloy nanoparticles (NPs) through electroless plating. Finally, hollow Ni–P amorphous alloy NSs were achieved by removing silica template. Such a Ni catalyst exhibits much superior performances to Raney Ni catalyst during liquid-phase hydrogenation of sugars to sugar alcohols.

## 2. Experimental section

### 2.1. Catalyst preparation

*Chemicals and reagents.* All of the chemicals used in this experiment were obtained from commercial sources and used without any other treatments. Tetraethoxysilane (TEOS), aminopropyl triethoxysilane (APTES), chloroauric acid trihydrate ( $\text{HAuCl}_4 \cdot 3\text{H}_2\text{O}$ ), trisodium citrate dihydrate ( $\text{Na}_3\text{C}_6\text{H}_5\text{O}_7 \cdot 2\text{H}_2\text{O}$ ), sodium borohydride ( $\text{NaBH}_4$ ), nickel sulfate hexahydrate ( $\text{NiSO}_4 \cdot 6\text{H}_2\text{O}$ ), sodium hypophosphite dihydrate ( $\text{NaH}_2\text{PO}_2 \cdot 2\text{H}_2\text{O}$ ), sodium acetate ( $\text{CH}_3\text{COONa}$ ), nickel chloride ( $\text{NiCl}_2$ ) and ethanol were purchased from Aladdin Industrial Co., Ltd. (Shanghai, China).

*Synthesis of amine-functionalized silica NSs.* Aminopropyl group grafted silica NSs were synthesized through a modified Stöber method [42], and designated as  $\text{SiO}_2\text{-NH}_2$ . In a typical run of synthesis, TEOS (4.7 mL) were added in a mixture of ethanol (50 mL), deionized water (16 mL), and concentrated ammonia aqueous solution (28 wt%, 9.0 mL). After being stirred at 313 K for 2.5 h, APTES (0.2 mL) was added dropwise. After being stirring for 12 h, the solid product was collected and washed thoroughly with deionized water, followed by drying under vacuum at 353 K for 8 h.

*Synthesis of Ni-P/SiO<sub>2</sub>-NH<sub>2</sub> composites.* To generate crystal seeds, gold colloid NPs were synthesized according to the method reported by Jana et al. [43]. Briefly, a 150 mL aqueous solution containing  $2.5 \times 10^{-4}$  M  $\text{HAuCl}_4$  and  $2.5 \times 10^{-4}$  M  $\text{Na}_3\text{C}_6\text{H}_5\text{O}_7$  was firstly prepared. Next, 4.5 mL of 0.1 M  $\text{NaBH}_4$



solution was added dropwise to the solution at 273 K and was stirred continuously until no bubbles released. The as-prepared  $\text{SiO}_2\text{-NH}_2$  was then added into the above solution. After being stirred at 298 K for 12 h, the solid was centrifuged, washed thoroughly with deionized water, and dried under vacuum at 353 K for 8 h. The Au-modified  $\text{SiO}_2\text{-NH}_2$  NSs were added into an electroless plating bath containing 150 mL of plating solution with the composition as shown in Table 1. High-purity nitrogen was used as the sheltering gas. With stirring, electroless plating was carried out to generate Ni-P/ $\text{SiO}_2\text{-NH}_2$  composites under the reaction conditions (see Table 1). In this plating process,  $\text{NiSO}_4$  was used as the source of metal ions;  $\text{NaH}_2\text{PO}_2$  was used as a reducing agent;  $\text{Na}_3\text{C}_6\text{H}_5\text{O}_7$  was used as a complexing agent for  $\text{Ni}^{2+}$  in solution;  $\text{CH}_3\text{COONa}$  was used as buffering agent for pH control. The resultant Ni-P/ $\text{SiO}_2\text{-NH}_2$  composites were centrifuged and washed with deionized water for several times.

*Synthesis of hollow Ni-P amorphous alloy NSs.* The silica template was removed by refluxing the Ni-P/ $\text{SiO}_2\text{-NH}_2$  composites in 10 mL of 2 M NaOH solution at 313 K for 30 min, followed by washing thoroughly with deionized water until the pH reached 7. Finally, the solid was washed with ethanol three times and kept in ethanol until the time of use. The as-received sample is denoted as Ni-P-H, where the suffix “-H” means hollow structure.

*Reference catalysts.* For comparison, the reference Ni-P amorphous alloy NPs was also prepared by the regular method, i.e., by direct reduction of Ni

chloride with sodium hypophosphite [44]. In a typical synthesis, 21.0 mmol of NiCl<sub>2</sub>, 47.2 mmol of NaH<sub>2</sub>PO<sub>2</sub>, and 36.7 mmol of CH<sub>3</sub>COONa were dissolved in 100 mL of deionized water in a three-necked flask and maintained at 363 K. The resulting black precipitate was separated by centrifugation and washed with deionized water. Finally, the solid was washed with ethanol three times and kept in ethanol until the time of use. The as-received sample is denoted as Ni-P-S, where the suffix “-S” means solid structure. Raney Ni was commercially available from a sorbitol production factory in China and was used without additional activation.

## *2.2. Catalyst characterization*

The bulk compositions were analyzed by means of inductively coupled plasma optical emission spectrometry (ICP-OES; Varian VISTA-MPX). The amorphous structure was determined by X-ray diffraction (XRD; Rigaku D/Max-RB with Cu K $\alpha$  radiation). Solid-state nuclear magnetic resonance (NMR) spectra were collected on a Bruker AV-400 NMR spectrometer. Fourier transform infrared (FTIR) spectra were recorded on a Nicolet Magna 550 spectrometer by KBr technique. Thermogravimetric analysis and differential thermal analysis (TG/DTA) were conducted on a Shimadzu DTG-60 TG/DTA analyzer with a ramping rate of 10 K min<sup>-1</sup> in 50 mL min<sup>-1</sup> of air flow. The catalyst shapes and morphologies were observed by both field emission scanning electron microscopy (FESEM; HITACHI S-4800) and transmission

electron microscopy (TEM; JEOL JEM2100). The surface electronic states were investigated by X-ray photoelectron spectroscopy (XPS; ULVAC-PHI PHI5000 VersaProbe using Al K $\alpha$  radiation), during which all samples were dried and pretreated *in situ* in pure Ar atmosphere to avoid oxidation. N<sub>2</sub> adsorption-desorption isotherms were obtained at 77 K using a Quantachrome NOVA 4000e apparatus. By N<sub>2</sub> adsorption, the Brunauer-Emmett-Teller (BET) surface area ( $S_{\text{BET}}$ ) was calculated by using the multiple-point BET method in the relative pressure range of  $P/P_0 = 0.05-0.2$ . The pore size distribution curve (calculated from the adsorption isotherm) was obtained by the Barrett-Joyner-Halenda (BJH) model. The active surface area ( $S_{\text{act}}$ ) was measured by the hydrogen chemisorption at room temperature, which was performed on a Micromeritics AutoChem II 2920 instrument using a dynamic pulse method. The sample was purged under an argon flow (purity of 99.997%, treated with an Alltech Oxy-Trap column) at 523 K for 2 h. The pretreated sample was cooled down to room temperature under argon atmosphere, and hydrogen pulses were injected at 303 K until the calculated areas of consecutive pulses were constant. According to the hydrogenation chemisorption,  $S_{\text{act}}$  of the as-prepared catalyst was calculated assuming Ni/H = 1 and a Ni surface of  $6.5 \times 10^{-20}$  m<sup>2</sup> per Ni atom [45]. Every sample was measured for three times. The reproducibility of the results was checked by repeating the measurements for three times on the same catalyst and was found to be within acceptable limits ( $< \pm 2\%$ ). The hydrogen

temperature-programmed desorption (H<sub>2</sub>-TPD) curve was obtained on the same instrument in Ar flow at a ramping rate of 20 K min<sup>-1</sup>.

### 2.3. Catalytic performances test

The liquid-phase hydrogenation of sugar was performed at 4.0 MPa of H<sub>2</sub> pressure and 373 K in a 200-mL stainless steel autoclave with a Teflon tube to avoid metal contamination, in which 0.5 g of Ni catalyst and a sugar aqueous solution (10 wt.% in 50 mL H<sub>2</sub>O) were well mixed. According to the drop of the H<sub>2</sub> pressure in the autoclave within 10 min, both the specific activity (the H<sub>2</sub> uptake rate per gram of Ni,  $R_{H^m}$ , mmol h<sup>-1</sup> g<sub>Ni</sub><sup>-1</sup>) and the intrinsic activity (the H<sub>2</sub> uptake rate per m<sup>2</sup> of Ni,  $R_{H^s}$ , mmol h<sup>-1</sup> m<sub>Ni</sub><sup>-2</sup>) were calculated by using the ideal gas equation. The reaction mixture was sampled at intervals for product analysis through a liquid-phase chromatograph (Agilent 1200) equipped with a carbohydrate column (Shodex, SC1011) and a refractive index detector at 333 K with water as movable phase at 0.50 mL min<sup>-1</sup>. Preliminary kinetic studies revealed that there was a plateau in the dependency of the reaction initial rate upon the stirring rate above 1000 rpm and that the reaction initial rate varied linearly with catalyst amount from 0.1 to 1.0 g, indicating that the stirring rate of 1200 rpm was high enough that the hydrogenation rates were independent of mass transfer. After cooling to room temperature at the end of the reaction, the catalyst was separated by centrifugation and washed with deionized water for further characterizations and applications. In order to determine the

catalyst durability, the used catalyst was centrifuged and washed thoroughly with distilled water after each run of the reaction. Then, the used catalyst was reused with fresh charge of sugar for subsequent recycle runs under same reaction conditions.

### 3. Results and discussion

#### 3.1. Catalyst characterization

As shown in FESEM image (Fig. S1), the as-prepared  $\text{SiO}_2\text{-NH}_2$  material is present in the form of uniform spheres with an average diameter around 230 nm, which is similar to the previously reported silica spheres [42]. The FTIR spectrum in Fig. S2 reveals that, besides the absorbance band at  $1088\text{ cm}^{-1}$  indicative of Si–O stretching vibration,  $\text{SiO}_2\text{-NH}_2$  NSs displays two absorbance bands at  $2928$ ,  $2849$  and  $1495\text{ cm}^{-1}$  characteristic of asymmetric stretching, symmetric stretching and bending vibrations of aliphatic C–H bonds in the  $\text{NH}_2\text{-CH}_2\text{-CH}_2\text{-CH}_2\text{-}$  group [46]. Meanwhile, the absorbance band at  $1522\text{ cm}^{-1}$  corresponding to the bending vibration of N–H bond is also clearly observed, though the N–H stretching vibration peak at  $3300\text{ cm}^{-1}$  is overlapped by O–H vibration at  $3500\text{ cm}^{-1}$  [46]. These results demonstrated the successful incorporation of aminopropyl groups into the silica network, which could be further confirmed by the solid-state NMR spectra. The  $^{29}\text{Si}$  CP MAS NMR spectrum (Fig. S3) of the as-made  $\text{SiO}_2\text{-NH}_2$  NSs shows three well-resolved up-field resonance peaks for the siloxane corresponding to  $\text{Q}^4$  ( $\delta = -110\text{ ppm}$ ),  $\text{Q}^3$

( $\delta = -100$  ppm) and  $Q^2$  ( $\delta = -91$  ppm), where  $Q^n = \text{Si}(\text{OSi})_n(\text{OH})_{4-n}$  ( $n = 2-4$ ). Meanwhile, two down-field organosilane signals were observed at  $-65$  and  $-56$  ppm, corresponding to  $T^3$  and  $T^2$ , where  $T^m = \text{RSi}(\text{OSi})_m(\text{OH})_{3-m}$  ( $m = 1-3$ ), which demonstrated the incorporation of the organic groups into the silica framework *via* forming C-Si bond [46]. Additionally, the TGA/DTA curves (Fig. S4) reveal that, besides the weight loss before 473 K due to the desorption of physically adsorbed solvents,  $\text{SiO}_2\text{-NH}_2$  NSs displays weight loss between 473 and 873 K, corresponding to the oxidation removal of the organic groups anchored on  $\text{SiO}_2\text{-NH}_2$  NSs.

Due to the growth of highly isotropic structure, the Ni-P sample prepared *via* conventional chemical reduction method displayed regular spherical particles with the average size around 70 nm (Fig. S5). By using the surface-activated host materials, however, selective deposition of Ni-P can be achieved through electroless plating method. The TEM image (Fig. 1a) shows that the Ni-P/ $\text{SiO}_2\text{-NH}_2$  composites synthesized through the present method was monodisperse and with uniformly spherical NPs with an average particle size around 250 nm. A close view of these NSs by TEM (Fig. 1b) reveals a compact Ni-P overlayer with 25 nm thickness was readily formed on the surface of  $\text{SiO}_2\text{-NH}_2$ , confirming the deposition of Ni-P on the host material. The TEM morphology (Fig. 1c) demonstrate that Ni-P-H is present in the form of uniformly spheres with the average diameter around 250 nm, almost the same as the diameter of  $\text{SiO}_2\text{-NH}_2$  NSs. Meanwhile, TEM observation of Ni-P-H

shows clear contrast difference between the center and the edge, indicating the inner of these spheres is hollow. From the high-magnification TEM image of a single Ni-P-H nanosphere in Fig. 1d, a shell thickness of 28 nm could be measured. Moreover, one can observe that the outer shell of Ni-P-H was comprise of uniform NPs with an average size of 3 nm. Fig. 2a shows N<sub>2</sub> adsorption-desorption isotherms of Ni-P-H sample. Notably, Ni-P-H exhibited a hysteresis loop at the relative pressure range of 0.4–1.0, which was assigned to mesopores formed through the pileup of Ni-P NPs. Ni-P-H also displayed a narrow pore size distribution centered around 3.5 nm (Fig. 2b), which was consistent with the observation from high-magnification TEM image (Fig. 1d).

ICP analysis (Table 1) revealed that the bulk atom composition of Ni-P-H (Ni<sub>79</sub>P<sub>21</sub>) was almost exactly the same as that of the conventionally-prepared Ni-P-S (Ni<sub>80</sub>P<sub>20</sub>), suggesting the different preparation methods had no significant influence on the P contents in the final samples. Generally, the P content has great effect on the structural properties of Ni-P sample. More specifically, the Ni-P was amorphous when the P content is higher than 10 mol%, while lower P content resulted in a mixture of amorphous Ni-P and face-centered cubic Ni [27]. The SAED image presented in Fig. 1e shows a successive diffraction halo, suggesting that the Ni-P-H synthesized *via* the present method was present in a typical amorphous alloy structure [27]. The amorphous alloy structure of Ni-P-H can be further confirmed by the XRD

pattern (Fig. 3a), where only one broad peak centered at  $2\theta = 44^\circ$  was observed [27]. Heat treatment of the fresh Ni-P-*H* sample (at 673 K in N<sub>2</sub> for 2 h) resulted in the appearance of several diffraction peaks corresponding to metallic Ni and the crystalline Ni-P alloy (Fig. 3b). The appearance of Ni-P crystalline phases during the crystallization process verified the formation of an alloy between Ni and P for the as-synthesized Ni-P-*H*. We infer that except for the crystallization, partial decomposition of a Ni-P amorphous alloy may occur in this process. Similarly, considering the combined results from both the SAED (insert in Fig. S5) and the XRD (Fig. S6), Ni-P-*S* was identified to be amorphous alloy.

Fig. 4 shows the XPS spectrum of Ni-P-*H* sample. Only one peak around a BE at *ca.* 853.1 eV was observed in the Ni  $2p_{3/2}$  level (Fig. 4a). In comparison with the standard pure nickel, no significant change in the BE of the Ni  $2p_{3/2}$  level was observed, indicating that almost all of the nickel species in Ni-P-*H* were present as metallic state. This observation is in agreement with our previous results [27]. But, the phosphorus species in Ni-P-*H* sample were present in both the oxidized state and elemental state, corresponding to BE of around 133.6 and 130.0 eV (Fig. 4b), respectively, in P  $2p$  level. In comparison with Ni-P-*H*, Ni-P-*S* reveals nearly the same XPS spectrum (Fig. S7). The surface composition was determined by analysis of relative peak areas in the XPS spectra. According to the calculation based on XPS peak areas, the surface atomic ratio of the alloying P to the metallic Ni in Ni-P-*H* is 16/84, similar to



that in Ni-P-S (17/83). This means the nature of Ni active sites in both the Ni-P-H and the Ni-P-S is identical, regardless of the different preparation methods.

### 3.2. Catalytic performances

Initially, the liquid-phase hydrogenation of glucose to sorbitol under 4.0 MPa of hydrogen and 373 K is used for evaluating the performances of the as-synthesized catalysts. The reaction profiles (Fig. 5) reveal that Ni-P-H was extremely selective to sorbitol (nearly 100% throughout the reaction process). It should be noted that, all the Ni-based catalysts displayed 100% selectivity towards sorbitol under the present reaction conditions.

Table 1 summarizes some structural and catalytic parameters of the different catalysts during liquid-phase glucose hydrogenation. Although the commercial Raney Ni possessed a much higher  $S_{\text{act}}$  than all the Ni-based catalysts, it still displayed a much lower  $R_{\text{H}}^{\text{m}}$  and glucose conversion within 4 h because of its extremely lower intrinsic activity ( $R_{\text{H}}^{\text{s}}$ ). The superior  $R_{\text{H}}^{\text{s}}$  of the as-prepared Ni-P-H and Ni-P-S catalysts could be linked to their unique amorphous alloy structure, which had proven to be favorable for hydrogenation processes [27]. More specifically, the unique short-range ordering but long-range disordering amorphous structure endowed Ni-P amorphous alloy with a stronger synergistic effect between Ni active sites and more highly unsaturated Ni active sites than the crystalline catalyst, which may promote the adsorption

of reactants and favor hydrogenation activity [27]. This could be also supported by the fact that an abrupt decrease in activity was observed for the Ni-P-*H* treated at 673 K for 2 h in N<sub>2</sub> flow (Table 1), which was firstly due to the significant agglomeration of Ni-P NPs at elevated temperatures and, thus, decreasing metallic area ( $S_{\text{act}}$ ) and, secondly, the decrease in  $R_{\text{H}}^{\text{S}}$  resulted from the crystallization of Ni-P amorphous alloy. In addition, the presence of phosphorus oxide could further enhance the adsorption for glucose molecule *via* abstraction of proton, thereby favoring the subsequent hydrogenation of the reactant.

Based on the  $R_{\text{H}}^{\text{m}}$  and glucose conversion data presented in Table 1, it is obvious that the reactivity of Ni-P-*H* was more active than Ni-P-*S*. This could be attributed to both the larger  $S_{\text{act}}$  and the enhancement of  $R_{\text{H}}^{\text{S}}$ . The larger  $S_{\text{act}}$  of Ni-P-*H* compared to Ni-P-*S* could be interpreted in terms of the promotional effect of the hollow structure. Such nanoporous nature of the spherical chamber allowed reactant molecules to be adsorbed on both the outer shell and the interior shell of Ni-P-*H*, which might increase the accessibility and provide much more Ni active sites for reactant molecules, apparently favorable for hydrogenation. Apart from the larger specific surface area, Ni-P-*H* has larger  $R_{\text{H}}^{\text{S}}$  compared to its corresponding dense counterpart (Ni-P-*S*). Because both the Ni-P-*H* and the Ni-P-*S* catalysts possess similar compositions, amorphous alloy structure, as well as surface electronic characteristics, the distinct difference in morphology should be considered to

be responsible for the diverse  $R_{H^S}$ . The use of nonconvex-structured materials has been a hot frontier subject in recently years [47]. Noble-metal nanocrystals with concave surface have displayed great potential to serve as excellent catalysts due to their unique surface structure [48-52]. Ding's group inferred that the negative curvature of the inner surface in Ni-based catalysts provides more active centers for the reactant molecules and thus, favoring the catalytic hydrogenation [49]. To get insight into the different surface features between Ni-P-H and Ni-P-S, the two catalysts were subjected to H<sub>2</sub>-TPD. Apparently, both the Ni-P-H and the Ni-P-S catalysts display analogous H<sub>2</sub>-TPD profiles (Fig. 6), indicative of the presence of chemisorbed hydrogen species with similar adsorption energies. Compared with the H<sub>2</sub>-TPD profile of Ni-P-S, the desorption peak observed from Ni-P-H shifts markedly to a lower temperature, suggesting that the adsorption strength of hydrogen over the surface of Ni-P-H decreases. From this, we could deduce the existence of more electron-enriched surface, maybe due to the deviation from planarity. Generally, the concave metal surface possesses more active centers, which results into increase in electron density and weakens the strength of the hydrogen adsorption. Beenackers et al. confirmed that, upon adsorption of glucose on metals, an ionized species is generated (*i.e.* glucose anion), which was susceptible to attack by hydrogen adsorbed dissociatively on the neighboring metal sites, initiating the reaction [53]. Meanwhile, Wit et al. showed the promotional effect of proton abstraction from the anomeric hydroxyl group on the hydrogenation of glucose

[54]. The adsorption and hydrogenation of the glucose molecule on the inner surface of Ni-P-H could be described in the following model schematized in Scheme 3. Consequently, the Ni active sites in the inner surface of Ni-P-H with more electron is anticipated to readily abstract proton from glucose. On the other hand, the higher electron density on Ni active sites might facilitate the formation of H<sup>-</sup> species [55], which could promote glucose hydrogenation activity.

Additionally, the shells of Ni-P-H are nanoporous, which is expected to enhance the efficiency of mass transport in liquid-phase reaction. To closer look into the influence on the diffusion of reaction molecules, hydrogenation of maltose (Scheme 4), a bigger sugar molecule, was performed under the same reaction conditions as those for glucose hydrogenation. From the results tabulated in Table 3, one can see that all the Ni-P catalysts displayed 100% selectivity towards maltitol. Nonetheless, only 75% selectivity was obtained on the commercial Raney Ni catalyst because of the formation of sorbitol and an uncertain byproduct in small amount. Sorbitol could be considered as the hydrogenation product of glucose stemmed from the hydrolysis of maltose [30], and the uncertain byproduct was possibly formed *via* the dehydration reaction between glucose molecules and maltitol molecules [30]. The poor selectivity of Raney Ni could be attributed to the existence of residual alumina, which served as acidic sites to catalyze the hydrolysis of maltose and the condensation between glucose and maltitol [30]. Meanwhile, the commercial Raney Ni

catalyst displayed much lower  $R_{H^m}$  and conversion during maltose hydrogenation compared with those in glucose hydrogenation. This could be attributed to the presence of micropores in Raney Ni, which is unfavorable for catalytic activity in liquid-phase reaction owing to the mass transfer. Hardly, any difference in the catalytic efficiency for glucose hydrogenation and maltose hydrogenation could be found using Ni-P-S, apparently due to the absence of mass transfer limitation over Ni-P-S with dense structure. It should be noted that the run performed using Ni-P-H for maltose hydrogenation delivers similar catalytic efficiency to that for glucose hydrogenation. Apparently, the porous shells in Ni-P-H offer a convenient path for the big reactant molecules crossing into the inner surface for hydrogenation to maltitol.

Industrial application of a heterogenous catalyst greatly relies on its handling convenience and stability. During the liquid-phase hydrogenation of glucose, Ni-P-H could be easily separated from the reaction solution *via* centrifugation and used repetitively at least for 6 times without significant decrease of sorbitol yield (Fig. 7a). However, a remarkable loss in activity (30%) was observed for Ni-P-S after six recycles (Fig. 7a). During the liquid-phase hydrogenation of maltose, likewise, the maltitol yield decreases by 35% over Ni-P-S after 6 consecutive runs (Fig. 7b), whereas Ni-P-H could be used repetitively 6 times with slight loss of activity for maltose hydrogenation (9%) (Fig. 7b). ICP analysis revealed that no leaching of Ni species could be detected in the reaction mixtures for Ni-P-H and Ni-P-S catalysts during repeated use,

implying that both catalysts were stable against the chelating effect of reactant and product. TEM image of the used catalyst after 6 cycles (Fig. 8a) reveal that the deactivation of Ni-P-S can be due to a severe agglomeration of Ni-P NPs. However, the hollow chamber of Ni-P-H is stable, since part of the hollow spherical structure can be preserved after being used 6 times (Fig. 8b). According to these observation, the high durability of Ni-P-H can be attributed to its large diameter of hollow nanospheres, which facilitates separation from solution *via* centrifugation and diminishes the loss of catalyst during recycling tests. On the other hand, its self-supporting capacity is another factor responsible for the high durability of Ni-P-H, which retards the Ni-P NPs from agglomeration during the hydrogenation process.

#### 4. Conclusions

In summary, hollow structured Ni-P amorphous alloy nanospheres were synthesized through Ni electroless plating on aminopropyl-functionalized silica nanospheres, followed by removing silica template in NaOH solution. In particular, the present method is more facile and cost-effective. During liquid-phase hydrogenation of sugars to sugar alcohols, the synthesized hollow Ni-P amorphous alloy nanospheres delivered much superior catalytic performances to the dense Ni-P amorphous alloy and Raney Ni catalyst. These results not only greatly extend the application of amorphous alloy but also highlight the role of the significant catalysis from the unique concave surface. This strategy

can potentially be extended to other hollow metallic nanospheres with different composition and diameter, providing highly efficient catalysts for some reactions.

Credit Author Statement

We declare that we have no competing financial interests or personal relationships that could have appeared to influence the work reported in this paper.

## **Acknowledgement**

This work was supported by the National Natural Science Foundation of China (21972093, 21677098), Shanghai government (19SG42, 19520710700 and 18230742500), the Program for Professor of Special Appointment (Eastern Scholar) at Shanghai Institutions of Higher Learning (TP2016034), the Ministry of Education of China (PCSIRT\_IRT\_16R49) and Shanghai Engineering Research Center of Green Energy Chemical Engineering (18DZ2254200).

## **Appendix A. Supplementary material**

Supplementary data associated with this article can be found, in the online version, at <http://dx.doi.org/>

## **References**

[1] A. Corma, S. Iborra, A. Velty, *Chem. Rev.* 107 (2007) 2411.

- [2] R. Rinaldi, F. Schüth, *Energy Environ. Sci.* 2 (2009) 610.
- [3] D.A. Simonetti, J.A. Dumesic, *Catal. Rev. Sci. Eng.* 51 (2009) 441.
- [4] J.C. Serrano-Ruiz, J.A. Dumesic, *Energy Environ. Sci.* 4 (2011) 83.
- [5] M. Besson, P. Gallezot, C. Pinel, *Chem. Rev.* 114 (2014) 1827.
- [6] H. Yue, Y. Zhao, X. Ma, J. Gong, *Chem. Soc. Rev.* 41 (2012) 4218.
- [7] X. Liu, X. Wang, S. Yao, Y. Jiang, J. Guan, X. Mu, *RSC Adv.* 4 (2014) 49501.
- [8] J. Kadokawa, *Chem. Rev.* 111 (2011) 4308.
- [9] L. Xu, W. Wei, H.X. Li, H. Li, *ACS Catal.* 4 (2014) 251.
- [10] W. Wei, Y. Zhao, S. Peng, H. Zhang, Y. Bian, H.X. Li, H. Li, *ACS Appl. Mater. Interfaces* 6 (2014) 20851.
- [11] M. Katz, E.E. Reese, *Appl. Microbiol.* 12 (1968) 419.
- [12] W. Wei, C. Wang, Y. Zhao, S. Peng, H. Zhang, Y. Bian, H.X. Li, X. Zhou, H. Li, *J. Catal.* 327 (2015) 78.
- [13] T. Werpy, G. Peterson, *Top value added chemicals from biomass, vol. 1: results of screening for candidates from sugars and synthesis gas*. US Department of Energy, Energy efficiency and renewable energy, Battelle, <http://www1.eere.energy.gov/biomass/pdfs/35523.pdf>.
- [14] P.L. Dhepe, F. Fukuoka, *Catal. Surv. Asia* 11 (2007) 186.
- [15] W.S. Fedor, J. Millar, A.J. Accola, *Ind. Eng. Chem.* 52 (1960) 282.
- [16] W.M. Kruse, L.W. Wright, *Carbohydr. Res.* 64 (1978) 293.
- [172] P. Gallezot, P.J. Cerino, B. Blanc, G. Fleche, P. Fuertes, *J. Catal.* 146 (1994) 93.



- [18] S. Kolaric, V. Sunjic, *J. Mol. Catal. A* 110 (1996) 189.
- [19] H. Li, H.X. Li, J.F. Deng, *Catal. Today* 74 (2002) 53.
- [20] B. Kusserow, S. Schimpf, P. Claus, *Adv. Synth. Catal.* 345 (2003) 289.
- [21] S. Schimpf, C. Louis, P. Claus, *Appl. Catal. A* 356 (2009) 112.
- [22] V.N. Sapunov, M.Y. Grigoryev, E.M. Sulman, M.B. Konyaeva, V.G. Matveeva, *J. Phy. Chem. A* 117 (2013) 4073.
- [23] S. Wang, W. Wei, Y. Zhao, H.X. Li, H. L, *Catal. Today* 258 (2015) 327.
- [24] B.W. Hoffer, E. Crezee, F. Devred, P.R. Mooijman, W.G. Sloof, P.J. Kooyman, A.D. van Langeveld, F. Kapteijn, J. A. Moulijn, *Appl. Catal. A* 253 (2003) 437.
- [25] I. Toufeili, S. Dziedzic, *Food Chem.* 47 (1993) 17.
- [26] Y. Pei, G.B. Zhou, N. Luan, B.N. Zong, M.H. Qiao, F. Tao, *Chem. Soc. Rev.* 41 (2012) 8140.
- [27] H. Li, W. Wei, Y. Zhao, H.X. Li, *Catalysis* 27 (2015) 144.
- [28] M. Wang, B. Feng, H. Li, H.X. Li, *Chem* 5 (2019) 805.
- [29] H. Li, P. Yang, D. Chu, H.X. Li, *Appl. Catal. A* 325 (2007) 34.
- [30] H. Li, D. Chu, J. Liu, M. Qiao, W. Dai, H.X. Li, *Adv. Synth. Catal.* 350 (2008) 829.
- [31] H.X. Li, W. Wang, J.F. Deng, *J. Catal.* 191 (2000) 257.
- [32] X. Wang, J. Feng, Y. Bai, Q. Zhang, Y. Yin, *Chem. Rev.* 116 (2016) 10983.
- [33] H. Li, J. Liu, S. Xie, M. Qiao, W. Dai, Y. Lu, H.X. Li, *Adv. Funct. Mater.* 18 (2008) 3235.

- [34] H. Li, Z. Zhu, J. Liu, S. Xie, H.X. Li, *J. Mater. Chem.* 20 (2010) 4366.
- [35] H. Li, Z. Zhu, H.X. Li, P. Li, X. Zhou, *J. Colloid Interf. Sci.* 349 (2010) 613.
- [36] H. Li, Y. Xu, J. Liu, Q. F. Zhao, H. X. Li, *J. Colloid Interface Sci.* 334 (2009) 176.
- [37] H. Li, D. Zhang, G. Li, Y. Xu, Y. Lu, H. X. Li, *Chem. Commun.* 46 (2010) 791.
- [38] W. Wei, Y. Zhao, S. Peng, H. Zhang, Y. Bian, H. X. Li, H. Li, *J. Mater. Chem. A* 2 (2014) 19253.
- [39] Y. Sun, Y. Xia, *Science* 298 (2002) 2176.
- [40] H. Li, H. Lin, Y. Hu, H. X. Li, P. Li, X. G. Zhou, *J. Mater. Chem.* 21 (2011) 18447.
- [41] X. Chen, W. Yang, S. Wang, M. Qiao, S. Yan, K. Fan, H. He, *New J. Chem.* 29 (2005) 266.
- [42] W. Stöber, A. Fink, E. Bohn, *J. Colloid Interface Sci.* 26 (1968) 62.
- [43] N.R. Jana, L. Gearheart, C.J. Murphy, *Langmuir* 17 (2001) 6782.
- [44] S. Xie, M. Qiao, W. Zhou, G. Luo, H. He, K. Fan, T. Zhao, W. Yuan, *J. Phys. Chem. B* 109 (2005) 24361.
- [45] J.J.F. Scholten, A.P. Pijers, A.M.L. Hustings, *Catal. Rev.: Sci. Eng.* 27 (1985) 151.
- [46] S. Wang, W. Wei, Y. Zhao, H.X. Li, H. Li, *Catal. Today* 258 (2015) 327.
- [47] Q. Chen, Y. Jia, S. Xie, Z. Xie, *Chem. Soc. Rev.* 45 (2016) 3207.

- [48] Y. Zhu, F. Liu, W. Ding, X. Guo, Y. Chen, *Angew. Chem. Int. Ed.* 45 (2006) 7211.
- [49] M. Mo, L. Han, J. Lv, Y. Zhu, L. Peng, X. Guo, W. Ding, *Chem. Commun.* 46 (2010) 2268.
- [50] Y. Jia, Y. Jiang, J. Zhang, L. Zhang, Q. Chen, Z. Xie, L. Zheng, *J. Am. Chem. Soc.* 136 (2014) 3748.
- [51] L. Zhang, L. T. Roling, X. Wang, M. Vara, M. Chi, J. Liu, S. I. Choi, J. Park, J. A. Herron, Z. Xie, M. Mavrikakis, Y. Xia, *Science*, 349 (2015) 412.
- [52] Q. Chen, Y. Yang, Z. Cao, Q. Kuang, G. Du, Y. Jiang, Z. Xie, L. Zheng, *Angew. Chem. Int. Ed.* 55 (2016) 9021.
- [53] G. de Wit, J.J. de Vlieger, A.C.K. Dalen, R. Heus, R. Laroy, A.J. Van Hengstum, A.P.G. Kieboom, H. Van Bekkum, *Carbohydr. Res.* 91 (1981) 125.
- [54] H. Noller, W.M. Lin, *J. Catal.* 85 (1984) 25.
- [55] J.A.W.M. Beenackers, B.F.M. Kuster, H.S. Van der Baan, *Carbohydr. Res.* 140 (1985) 169.

## Figure captions

**Scheme 1.** Catalytic hydrogenation of glucose to sorbitol.

**Scheme 2.** Schematic illustration of the formation of hollow Ni–P amorphous alloy nanospheres.

**Scheme 3.** Schematic representation of the reaction mechanism between adsorbed glucose and hydrogen on Ni–P-*H* amorphous alloy catalyst.

**Scheme 4.** Catalytic hydrogenation of maltose to maltitol.

**Fig. 1.** (a) TEM image of Ni–P/SiO<sub>2</sub>–NH<sub>2</sub>. (b) High-magnification TEM image of Ni–P/SiO<sub>2</sub>–NH<sub>2</sub>. (c) TEM image of Ni–P-*H*. (d) High-magnification TEM image of Ni–P-*H*. (e) SAED pattern of Ni–P-*H*.

**Fig. 2.** (a) N<sub>2</sub> adsorption-desorption isotherms and (b) pore size distribution of Ni–P-*H*.

**Fig. 3.** XRD patterns of (a) the fresh Ni–P-*H*, (b) the Ni–P-*H* treated at 673 K in N<sub>2</sub> flow for 2 h.

**Fig. 4.** XPS of Ni–P-*H*. (a) Ni 2*p* and (b) P 2*p*.

**Fig. 5.** Reaction profile of glucose hydrogenation over Ni–P-*H*. Reaction conditions are given in Table 2.

**Fig. 6.** H<sub>2</sub>-TPD profiles of (a) Ni–P-*H* and (b) Ni–P-*S*. The signal is normalized based on unit mass Ni.

**Fig. 7.** Recycling test of Ni–P-*H* and Ni–P-*S* catalysts for (a) glucose and (b) maltose hydrogenation. Reaction conditions are given in Table 2 and Table 3. Each run was conducted for 4 h in the recycling test.

**Fig. 8.** TEM image of (a) Ni–P-*S* and (b) Ni–P-*H* after six consecutive runs for maltose hydrogenation. Reaction conditions are given in Table 3. Each run was conducted for 4 h in the recycling test.

**Table 1** Electroless-plating bath composition and plating conditions

Concentrations and conditions	
$\text{NiSO}_4 \cdot 6\text{H}_2\text{O}$	0.076 mol/L
$\text{NaH}_2\text{PO}_2 \cdot 2\text{H}_2\text{O}$	0.19 mol/L
$\text{Na}_3\text{C}_6\text{H}_5\text{O}_7 \cdot 2\text{H}_2\text{O}$	0.017 mol/L
$\text{CH}_3\text{COONa}$	0.061 mol/L
pH	7.0
temperature	45°C
time	30 min

**Table 2** Structural characteristics and catalytic properties of the as-prepared catalysts during glucose hydrogenation<sup>a</sup>

Catalyst	Composition (at.%)	$S_{\text{act}}$ ( $\text{m}^2 \text{g}^{-1}$ )	$R_{\text{H}}^{\text{m}}$ ( $\text{mmol h}^{-1} \text{g}^{-1}$ )	$R_{\text{S}}^{\text{m}}$ ( $\text{mmol h}^{-1} \text{m}^{-2}$ )	Conversion (%)
Ni-P-H	Ni <sub>79</sub> P <sub>21</sub>	7.8	18.5	2.4	96
Ni-P-S	Ni <sub>80</sub> P <sub>20</sub>	4.7	9.42	2.0	88
Crystallized Ni-P-H <sup>b</sup>	Ni <sub>79</sub> P <sub>21</sub>	3.0	2.08	0.69	46
Raney Ni <sup>c</sup>	/	32.2	4.79	0.15	76

<sup>a</sup> Reaction conditions: 0.5 g catalyst, glucose aqueous solution (10 wt.%, 50 mL),  $T = 373 \text{ K}$ ,  $p_{\text{H}_2} = 4.0 \text{ MPa}$ , reaction time = 4 h, stirring rate = 1200 rpm.

<sup>b</sup> Obtained by treating the fresh Ni-P-H at 673 K under N<sub>2</sub> flow for 2 h.

<sup>c</sup> 1.0 g Raney Ni was used.

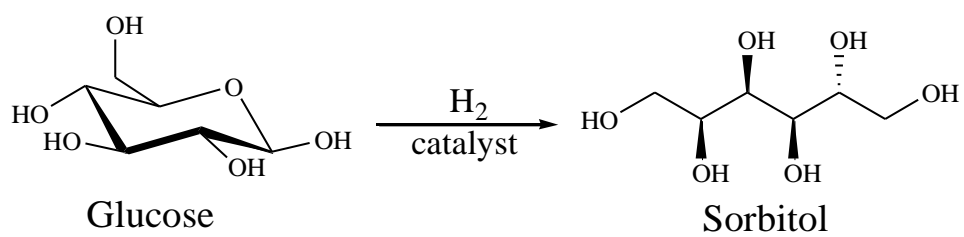
**Table 3** Catalytic properties of the as-prepared catalysts during maltose hydrogenation<sup>a</sup>

Catalyst	$R_H^m$ (mmol h <sup>-1</sup> g <sup>-1</sup> )	$R_S^m$ (mmol h <sup>-1</sup> m <sup>-2</sup> )	Conversion (%)	Selectivity (%)
Ni-P-H	17.6	2.3	95	100
Ni-P-S	9.65	2.1	86	100
Crystallized Ni-P-H <sup>b</sup>	2.01	0.67	43	100
Raney Ni <sup>c</sup>	3.70	0.11	66	75

<sup>a</sup> Reaction conditions: 0.5 g catalyst, maltose aqueous solution (10 wt.%, 50 mL),  $T = 373$  K,  $p_{H_2} = 4.0$  MPa, reaction time = 4 h, stirring rate = 1200 rpm.

<sup>b</sup> Obtained by treating the fresh Ni-P-H at 673 K under N<sub>2</sub> flow for 2 h.

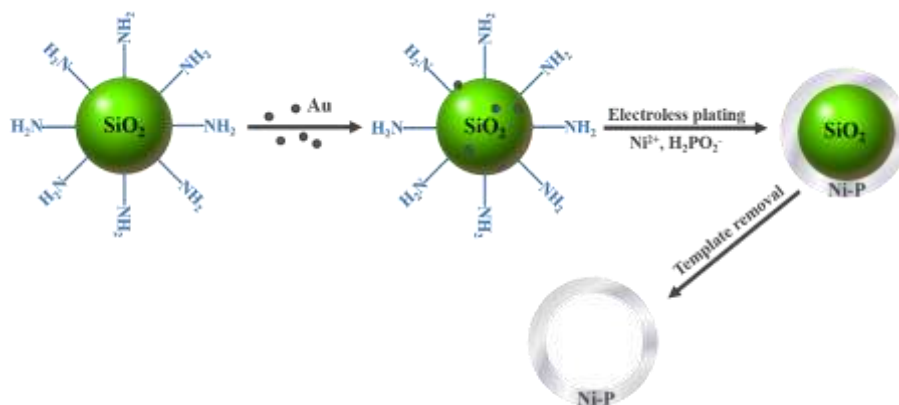
<sup>c</sup> 1.0 g Raney Ni was used.



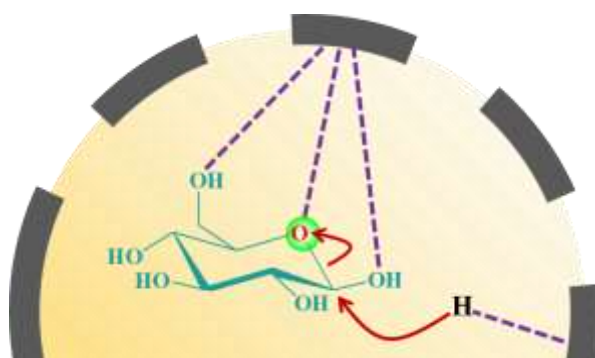
**Scheme 1.** Catalytic hydrogenation of glucose to sorbitol.

Journal Pre-proof



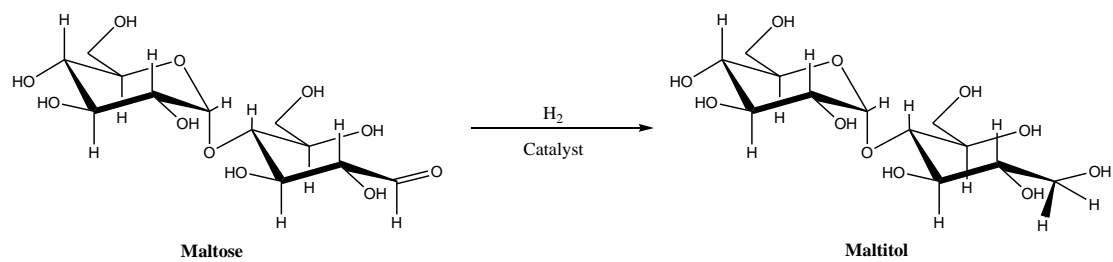


**Scheme 2.** Schematic illustration of the formation of hollow Ni-P amorphous alloy nanospheres.



**Scheme 3.** Schematic representation of the reaction mechanism between adsorbed glucose and hydrogen on Ni-P-H amorphous alloy catalyst.

Journal Pre-proof



**Scheme 4.** Catalytic hydrogenation of maltose to maltitol.

Journal Pre-proof

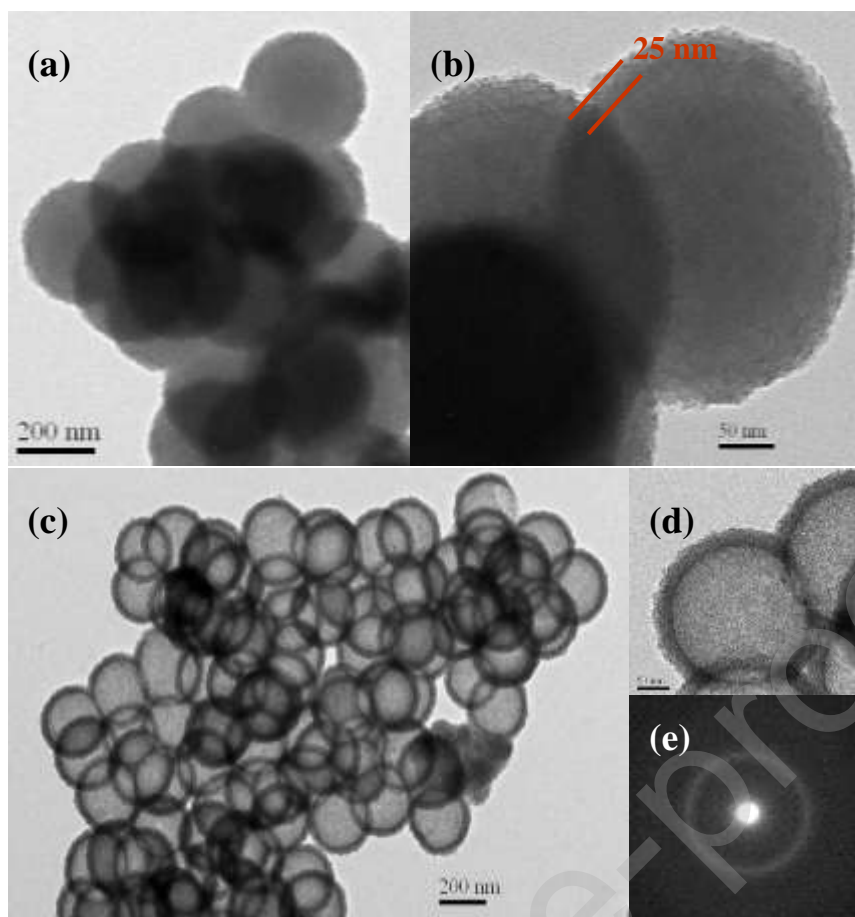


**Fig. 1.** (a) TEM image of Ni-P/SiO<sub>2</sub>-NH<sub>2</sub>. (b) High-magnification TEM image of Ni-P/SiO<sub>2</sub>-NH<sub>2</sub>. (c) TEM image of Ni-P-H. (d) High-magnification TEM image of Ni-P-H. (e) SAED pattern of Ni-P-H.

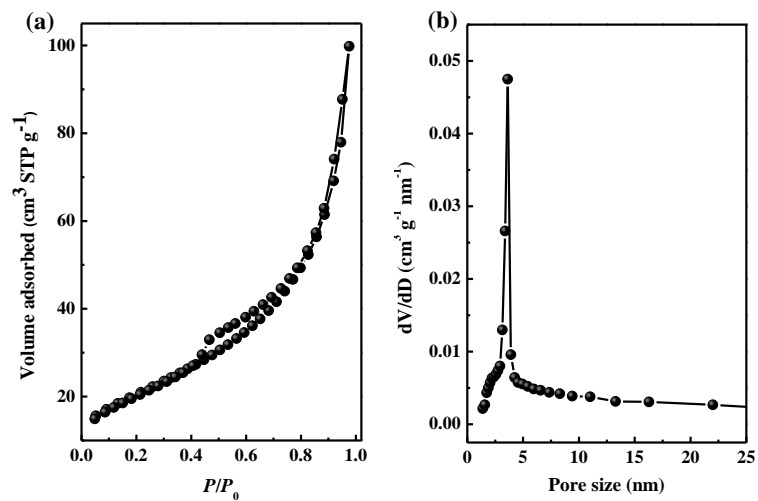


**Fig. 2.** (a) N<sub>2</sub> adsorption-desorption isotherms and (b) pore size distribution of Ni-P-H.

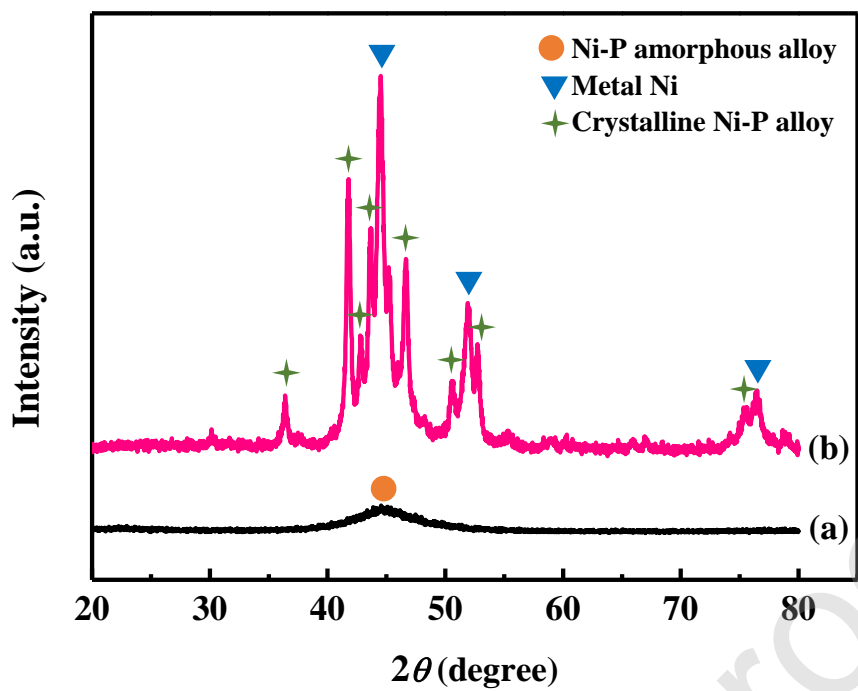


**Fig. 3.** XRD patterns of (a) the fresh Ni-P-H, (b) the Ni-P-H treated at 673 K in N<sub>2</sub> flow for 2 h.

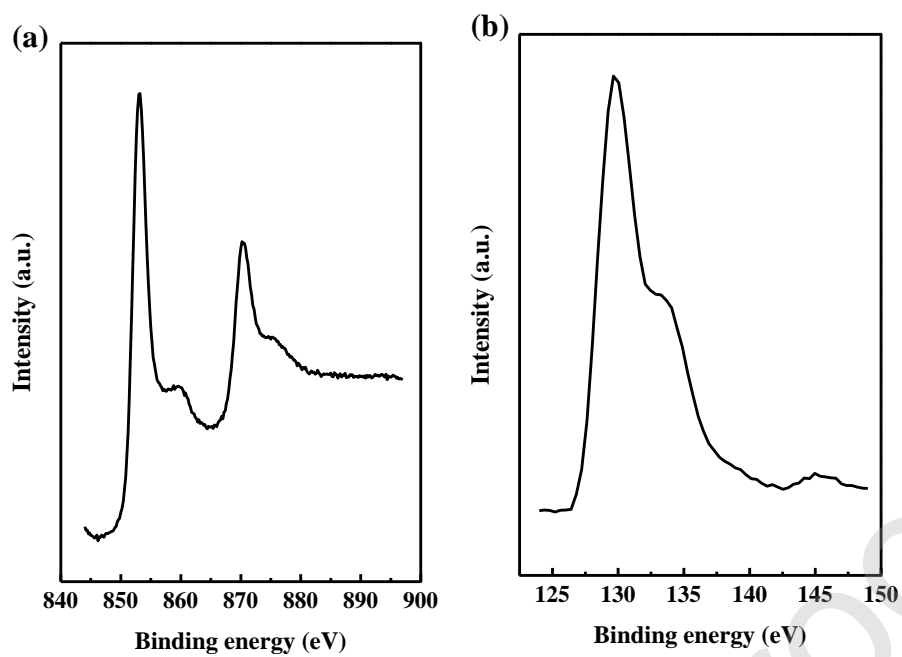


**Fig. 4.** XPS of Ni-P-H. (a) Ni 2p and (b) P 2p.

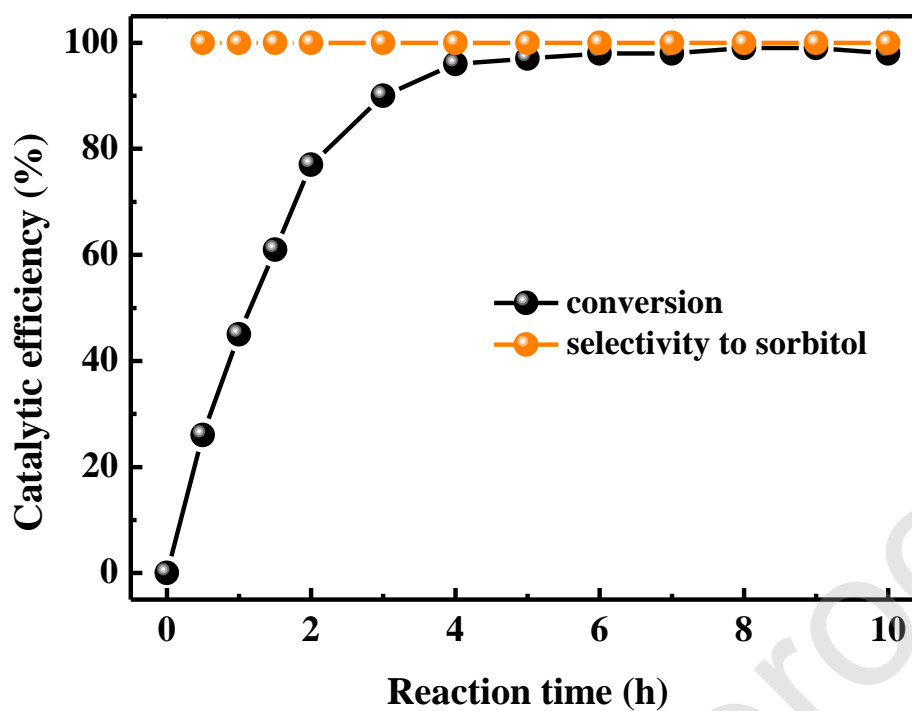


**Fig. 5.** Reaction profile of glucose hydrogenation over Ni-P-H. Reaction conditions are given in Table 2.



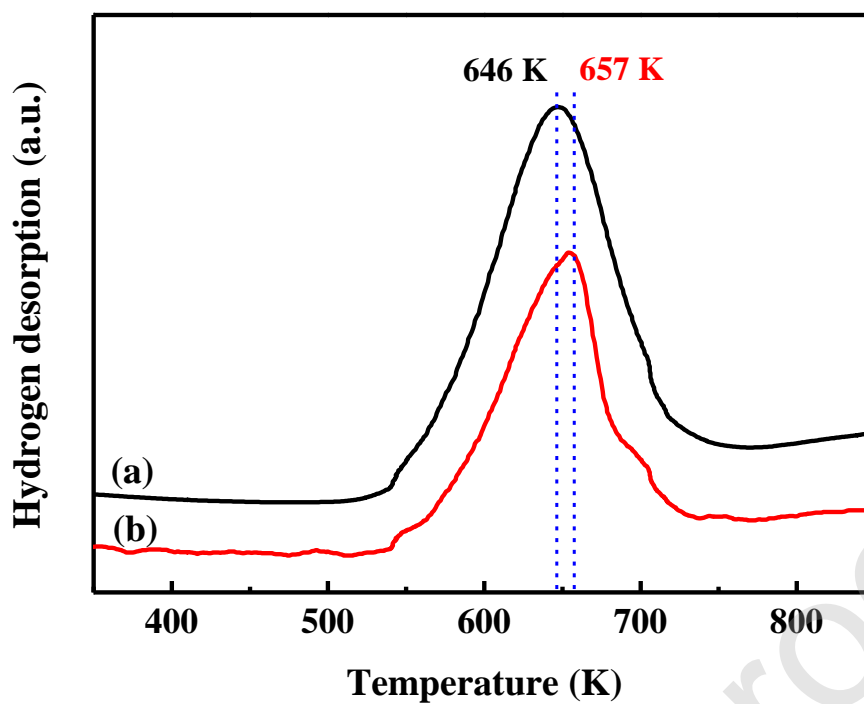


**Fig. 6.** H<sub>2</sub>-TPD profiles of (a) Ni-P-H and (b) Ni-P-S. The signal is normalized based on unit mass Ni.

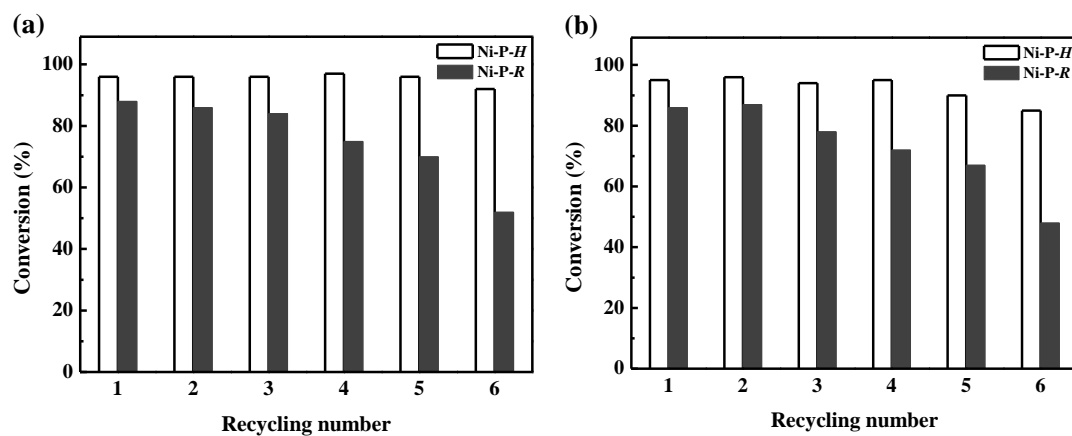


**Fig. 7.** Recycling test of Ni-P-H and Ni-P-S catalysts for (a) glucose and (b) maltose hydrogenation. Reaction conditions are given in Table 2 and Table 3. Each run was conducted for 4 h in the recycling test.

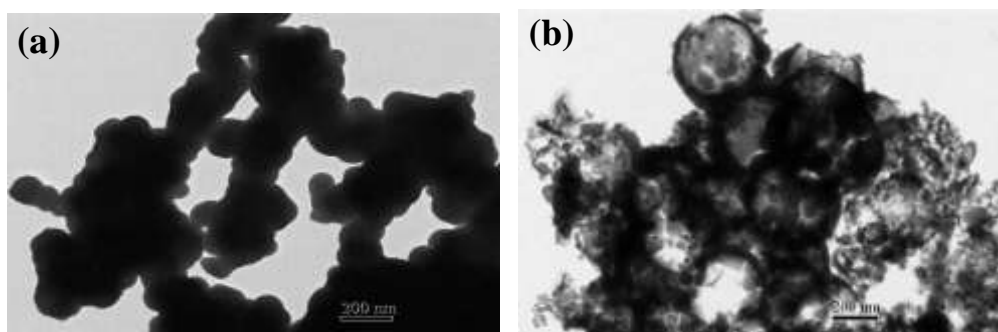


**Fig. 8.** TEM image of (a) Ni-P-S and (b) Ni-P-H after six consecutive runs for maltose hydrogenation. Reaction conditions are given in Table 3. Each run was conducted for 4 h in the recycling test.